Journal of the European Ceramic Society 16 (1996) 367–378

0955-2219(95)00193-X
0955-2219/96/$15.00

HREM of Ceramic High T_c Superconductors

G. Van Tendeloo & T. Krekels

EMAT, University of Antwerp (RUCA) Groenenborgerlaan 171, B-2020 Antwerp, Belgium

(Received 18 April 1995; revised version received 18 October 1995; accepted 24 October 1995)

Abstract

High resolution electron microscopy (HREM) is a real space technique, able to provide structural information complementary to the reciprocal space techniques such as X-ray or neutron diffraction. While the latter produce average information, HREM provides local information down to atomic scale. For ceramic high temperature superconductors not only the perfect structure is of importance, but particularly the defect structure or local structure. Physical properties such as critical current or superconducting volume fraction are strongly influenced by the deviations from perfection. We will further show that light element configurations—such as ogygen ordering or the incorporation of carbonate groups in the material—can be identified on atomic resolution images.

1 Introduction

Structural defects in materials strongly influence a large number of physical properties. Different techniques allow us to detect or characterize these defects in a direct or an indirect way. We may subdivide them in reciprocal space techniques, such as X-ray or neutron scattering, and real space techniques such as the different microscopy techniques.

The strength of reciprocal space techniques has been strongly improved recently because of synchrotron radiation sources; they allow a higher resolution and need smaller amounts of material. Neutron as well as X-ray diffraction are highly quantitative and detailed analyses of intensity maxima and peak widths allow us to draw far-reaching conclusions on the perfection of the material, deviations from stoichiometry, and the average defect density. However no direct visualization of these imperfections is possible and therefore important information such as a correlation between defects, Burgers vectors of dislocations, local deviations from perfection is not available. The presence of mesoscopic or nano-sized secondary phases as well as weak modulations in the structure can be easily overlooked.

Real space microscopy techniques can be subdivided into surface techniques and bulk techniques; both have their merits and specific application fields. Optical microscopy, scanning electron microscopy, scanning tunneling microscopy and atomic force microscopy for example belong to the former and give detailed, eventually atomic scale information on the surface perfection, surface reconstruction and surface adsorbtion. Information from the bulk can be obtained by a number of techniques such as acoustic microscopy, infra-red microscopy, X-ray tomography or others. Although most of these bulk techniques have their specific merits, the spacial resolution of the information is in general very limited however.

Electron microscopy not only has the advantage of being able to resolve structural details down to the atomic level, it also allows us to switch—with a single push-button—to electron diffraction, i.e. to reciprocal space. This combination of real space and reciprocal space information makes electron microscopy a unique technique for the study of solid state materials. As with all other techniques, it has its shortcomings and limitations, but electron microscopy can provide structural information that no other technique is able to produce.

We will illustrate the possibilities of HREM for several superconducting materials and we will emphasize especially the imaging of light elements such as oxygen and carbonate or sulphite groups.

2 Structural Defects in YBCO-Based Materials

The high temperature superconductor $YBa_2Cu_3O_7$ has been the first to be studied in detail by EM. The coherent twin fragmentation on (110) planes resulting from the tetragonal to orthorhombic phase transition was discovered by means of diffraction contrast electron microscopy and electron diffraction.[1,2] From a microstructural point

of view, $YBa_2Cu_3O_{7-\delta}$ is an interesting compound. It allows a large number of oxygen vacancies ($0 \leq \delta \lesssim 1$) on the oxygen sublattice. Depending on their concentration these vacancies tend to occur into various ordering schemes.[3–21] The $2a_0$ superstructure (Ortho II) in non-stoichiometric $YBa_2Cu_3O_{7-\delta}$, due to the alternation along the a_0 direction of filled and empty CuO chains in the CuO layers was also discovered by electron diffraction and electron microscopy.[3,17,18] The oxygen ordering occurs within nanometer size domains and is generally highly faulted; therefore it can hardly be detected by X-rays or neutrons. On the other hand these small dimensions make them eligible for flux pinning centra.

Another important feature of the YBCO compound is its susceptibility to allow elemental substitutions on most of its sublattices, without substantially altering the structure, but inducing quite different physical and chemical properties. We will focus here on those aspects where electron microscopy and electron diffraction have played an important role in elucidating the structure and bridging the gap between physical properties and structural data.

2.1 Oxygen-vacancy ordering in the CuO-plane of $YBa_2Cu_3O_{7-\delta}$

It is well-established that, at room temperature and atmospheric pressure, within the range $0 \leq \delta \lesssim \delta_t$ the structure of $YBa_2Cu_3O_{7-\delta}$ is orthorhombic and within the range $\delta_t \lesssim \delta \leq 1$, it is tetragonal. Values for δ_t vary around 0·65.[4,23–27] In experiments where δ is fixed the transition temperature T_t increases linearly with δ.[28] Reported values for the O $\rightarrow$ T transition temperature range between 110°C at $\delta = 0{\cdot}67$ and 680°C at $\delta = 0{\cdot}34$.

On cooling from the high temperature tetragonal phase, a spontaneous strain, proportional to the orthorhombicity of the material is introduced. This strain can be released by the introduction of coherent twinning on (110) planes. The microstructure then consists of slabs of two orientation variants of the orthorhombic phase. The (110) twinning is a reaction to a *macroscopic* orthorhombic strain. This, in contrast to the case of 'tweed' which seems to be triggered by *local* orthorhombic deformations. It is important to note that twinning as well as tweed are effects related to the orthorhombic range of the phase diagram. By non-local techniques such as X-ray or neutron diffraction, tweed textured material has often been described as tetragonal.

In the tetragonal phase, the oxygen atoms in the CuO-layer are distributed quasi randomly, with an equal occupation of the O(1)- and O(5)-sublattices. The sublattices consist of the oxygen sites between every two copper atoms in the plane, the O(1) sites lying along one direction (defined as *a*), the O(5) sites along the other (see Fig. 1). The formation of short CuO-segments along both basic directions of the CuO-chain plane is likely to cause local orthorhombic strains that lead to the pre-transition tweed texture.

The presence of short range ordering of oxygen and vacancies is revealed in electron diffraction

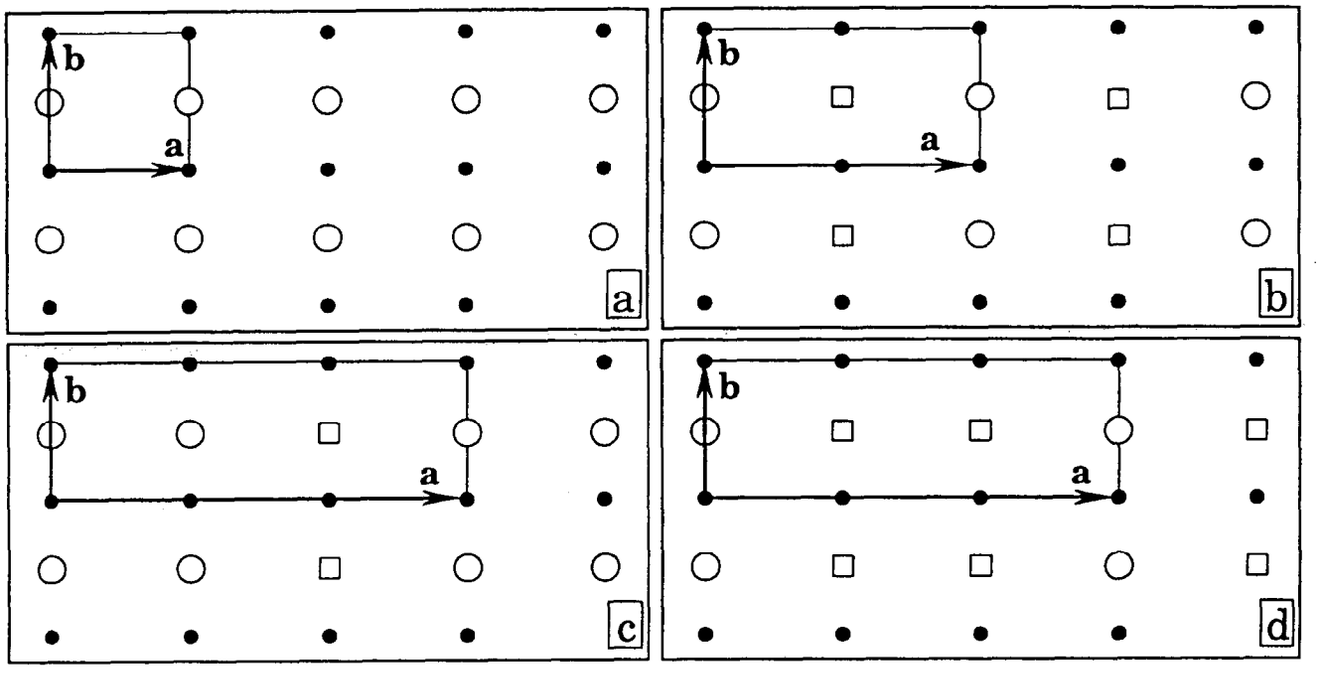

Fig. 1. (a) Schematic representation of the CuO-plane Ortho-I ordering. (b) Model of the Ortho-II ordering. Along a CuO and Cu-vacancy chains alternate. (c) and (d) are representations of ordering leading to tripled a-parameters: (c) represents the Ortho-III phase with an oxygen content 6·667; (d) represents a symmetric phase where roles of vacant and filled chains are reversed, that occurs at oxygen contents 6·333.

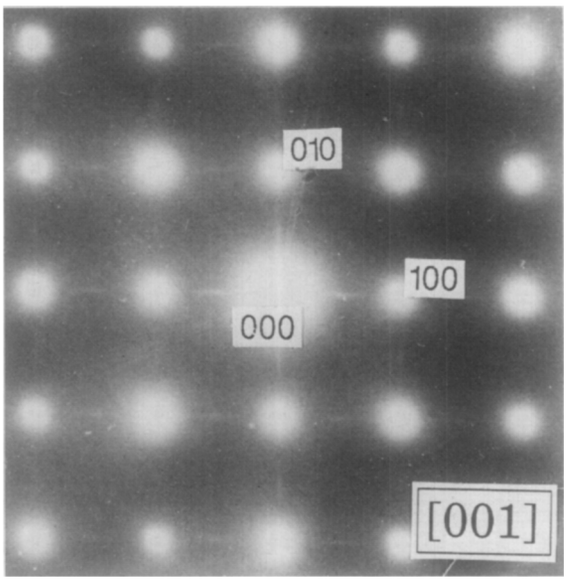

Fig. 2. Electron diffraction pattern along the [001] zone, in a tetragonal sample. *In situ* heating and cooling causes disorder reflected in the presence of diffuse scattering along the basic directions.

patterns by the occurence of diffuse intensities. The diffuse streaks observed in the [001]-zone diffraction pattern of Fig. 2 are due to the presence of irregularly spaced, short segments of CuO-chains. Short range order is commonly observed in highly oxygen deficient samples and can be induced in oxygen-rich materials by a thermal disordering by an *in situ* heating treatment.

The orthorhombic phase that corresponds to $YBa_2Cu_3O_7$ ($\delta = 0$), is termed 'Ortho-I'. The CuO-plane in the Ortho-I phase has all O(1)-sites filled and all O(5)-sites vacant. CuO-chains run along *b* (Fig. 1(a)). As a result, for the Ortho-I phase $a_o < b_o$. A second phase, termed Ortho-II, has every other *b*-oriented chain evacuated of oxygen and has an ideal composition $YBa_2Cu_3O_{6.5}$ ($\delta = 0.5$). (Fig. 1(b)) The oxygen content range over which the Ortho-II phase is observed stretches over $0.3 < \delta \leq 0.5$. The new unit mesh that can be defined on the ordered $CuO_{1-\delta}$-plane has dimensions $a_{II} = 7.668$ Å $\approx 2a_p$, $b_{II} = 3.869$ Å $\approx b_p$. (based on ref. 3). The Ortho-II-phase is easily recognized in [001] ED patterns (Fig. 3); it produces superstructure spots at positions $h + \frac{1}{2}\ k\ l$, characteristic for a doubling of the a-parameter. Often however, in such patterns also the b-parameter seems doubled by the appearance of spots at positions $h\ k + \frac{1}{2}\ l$ as well. These spots are due to the basic (110) twinning of the orthorhombic matrix, the resulting diffraction pattern (Fig. 3) being the overlap of the two identical patterns, with a rotation difference of about 90°. In ref. 29 it is shown that a disordered array of line defects gives rise to Lorentzian-shaped diffraction spots, with a position associated with the mean spacing of the scattering elements. When chains in the CuO-plane are irregularly spaced with a mean spacing of $2a_p$, Lorentzian shaped diffraction spots at positions $h + \frac{1}{2}\ k\ l$ are expected. When the average periodicity increases, the superstructure reflections will become more elongated. (Fig. 3(b)). A second factor influencing the superstructure reflection shape is the Ortho-II domain shape, small domain dimensions leading to elongated reflections. Intensity and sharpness of the superstructure reflections can thus be considered as indices of the domain size and the ordering quality of the phase. Whereas an ideal Ortho-II domain has an oxygen deficiency

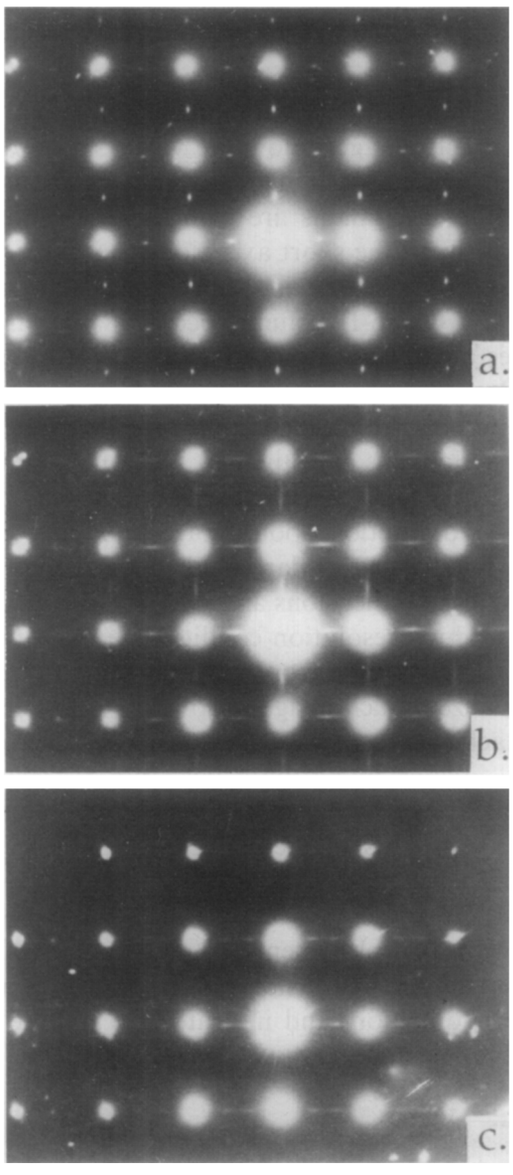

Fig. 3. (a) [001] zone diffraction pattern with sharp superstructure reflections at positions $h+\frac{1}{2}\ k\ l$ appearing in well-ordered Ortho-II material. Since the material is twinned, spots seem to appear along both basic directions. (b) [001] zone diffraction pattern with streaked superstructure intensity, corresponding to domains that are short range ordered along **a**, occurring at oxygen contents at the slopes above and below the Ortho-II plateau. (c) [001] zone diffraction pattern with spots at positions $h+\frac{1}{3}\ k\ l$ and $h+\frac{2}{3}\ k\ l$ due to an Ortho-III structure occurring in samples with oxygen contents around 6·8.

$\delta = 0{\cdot}5$, the strongest and sharpest Ortho-II electron diffraction intensity occurs at an oxygen deficiency of only $\delta = 0{\cdot}4$.[30] The domain size and the ordering quality thus are apparently maximized at $\delta = 0{\cdot}4$.

Dark field images allow the visualisation of the oxygen ordered domains. The images show that the Ortho-II domains are elongated or lenticular of shape, with the short axis along the *a*-direction. Largest Ortho-II domains (4 × 20 nm) and a maximal total Ortho-II volume, occur at oxygen deficiencies $\delta = 0{\cdot}4$. For the $\delta = 0{\cdot}4$ sample of ref. 5, from measurements of the Ortho-II peak surface in a [100] electron densitogram, the Ortho-II volume fraction was an estimated 50%, in accordance with our results. Samples showing elongated Ortho-II diffraction spots, correspondingly show Ortho-II domains in dark-field images (Fig. 4(b)) with reduced dimensions along *a* (size: 1 × 20 nm).

Under high resolution conditions, imaged along the [100] direction, the ordered domains can be easily visualized. Such images also allow us to deduce the stacking of the vacancy rows in successive $CuO_{1-\delta}$ planes along the *c*-axis (Fig. 5). The normal stacking of these rows is vertical, but small domains of a staggered stacking of successive 2D-ordered CuO-planes are no exception. The ordered domains also reveal anti-phase boundaries with a displacement vector $\mathbf{R} = \frac{1}{2}[100]_{OIIa}$. This is best visible under grazing angles along the [001] direction, and indicated by a white line, broken at the defects.

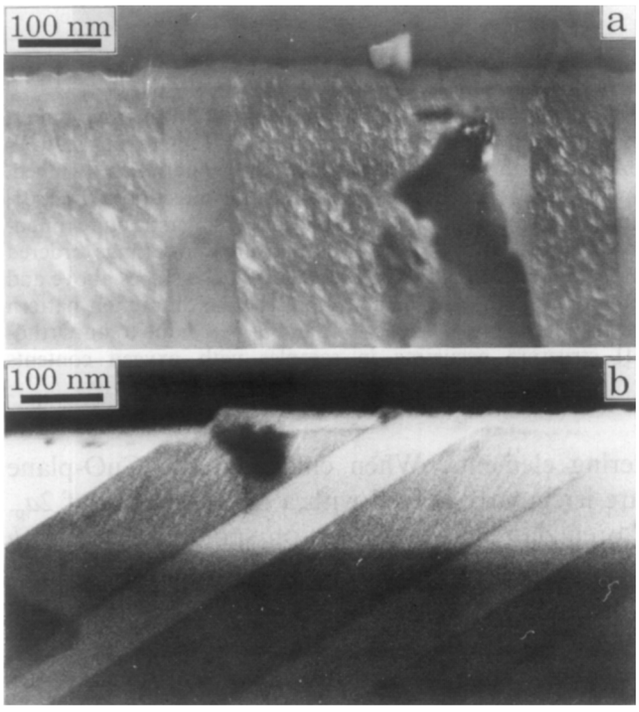

Fig. 4. (a) Dark field image showing Ortho-II ordered domains in bright. The corresponding diffraction pattern is shown in Fig. 3(a). (b) Dark field image corresponding to Fig. 3(b). Domain size is short along **a** and large along the CuO-chain direction **b**. The band structure in these images is due to twinning.

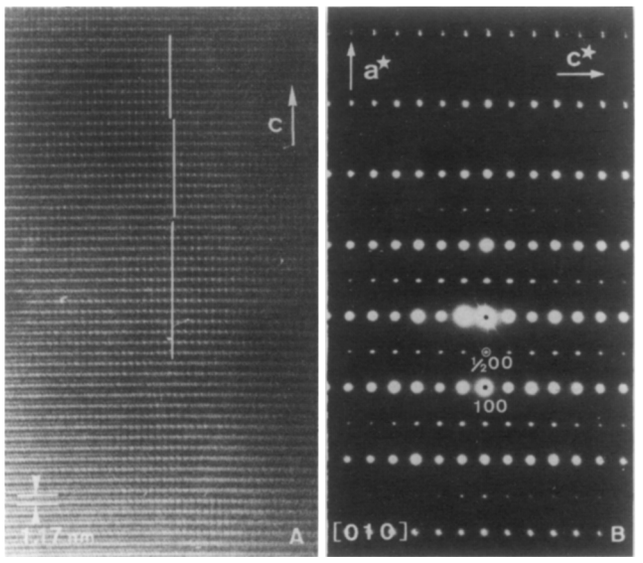

Fig. 5. (a) High resolution image along the [010]-axis, of the Ortho-II phase. The cell doubling can be seen by the white dots that appear every $2a_p$. In this view along the chains, chains are stacked vertically along **c**. Note the presence of anti-phase boundaries with displacement vector $\mathbf{R} = \frac{1}{2}[100]$. (b) Diffraction pattern along the [010] zone axis. Note the splitting of the outer spot rows due to twinning.

Instead of a doubling of the unit cell due to oxygen vacancy ordering along the *b*-axis, one can imagine different ordering schemes, introducing tripling, quadrupling, ... of the basic Ortho-I structure. Electron microscopic observations of the Ortho-III-phase have been reported (Fig. 3(c)), but much less and more ill defined than the Ortho-II phase.[10,31,32] Due to the short structural coherence length of this phase, their presence could not be detected neither by X-ray, nor by neutron diffraction. The Ortho-III phase ideally appears at an oxygen deficiency $\delta = \frac{1}{3}$, (or $\frac{2}{3}$) and compared to the Ortho-I phase, one out of three Cu_1O_1-chains is depleted of oxygen (Fig. 2(c)). Superstructures with longer periodicities of $4a_p$ and $5a_p$ have also been observed by electron microscopy.[33,34] These phases appear on very local scales (a few unit cells wide), and therefore have only been observed by means of high resolution electron microscopy. Identifying these phases as (Cu–O)-chain ordered phases, they should probably be considered as metastable phases at oxygen contents, intermediate to that of the stable Ortho-I, Ortho-II and Ortho-III phases. Theoretical studies seem to support this conclusion.[35,36]

2.2 (001) planar defects in YBCO-based material

The presence of (001) planar defects consisting of a double CuO-layer, replacing the normal single layer, was first demonstrated by means of electron microscopy[37] (Fig. 6). This observation has led to the development of a superconducting mixed layer Y–Ba–Cu–O family containing regular arrange-

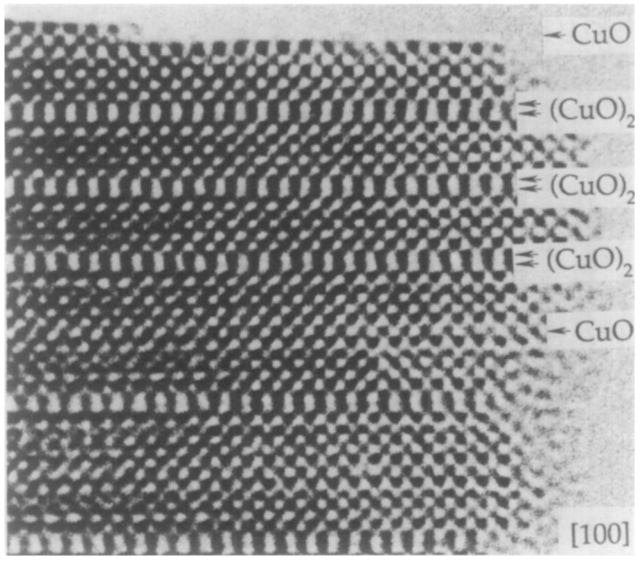

Fig. 6. HREM image showing the presence of double CuO planes in the $YBa_2Cu_3O_7$ structure.

ments of single and double CuO layers. Members of this family are the so called 1-2-4 phase ($YBa_2Cu_4O_8$)[38,39] and the 2-4-7 phase ($Y_2Ba_4Cu_7O_{15}$).[40] 1-2-4 and 2-4-7 can be regarded as members of a series of 'shear structures' derived from the 123 basic structure by the periodic insertions of supplementary CuO-layers. Representing the number of 123 unit cells separating these supplementary CuO-layers by an integer, the 124 and 247 structures are represented by the stacking symbols $1\bar{1}$ and $2\bar{2}$.[41,42] The minus sign is introduced to indicate that the presence of a double CuO layer causes a lateral offset between successive 123 blocks over ⅓[010]. High resolution images along the [010] direction of the perfect 124 and 247 structure are reproduced in Fig. 7(a, b). The double chain layers are characterized by intense rows of elongated double white dots. Changing the initial composition does not alter the stoichiometry of the outcoming material, one does however stabilize to some extent different phases such as $2\bar{2}$ and $3\bar{3}$ over limited areas. Figure 7(c) shows an example of a complex polytypoid over a limited region. Apart from this series of phases being a mixture of 1-2-3 and 1-2-4 where periodically double $(CuO)_2$ layers are introduced, a different series of Cu-rich phases was discovered, in which successive perovskite blocks are separated by triple $(CuO)_3$ layers.[43] An example is reproduced in Fig. 8 together with a schematic inset where the CuO layer configuration is represented by black dots. In some parts of the crystal even isolated CuO multilayers consisting of as much as five CuO layers have been observed in a matrix of essentially 2-4-7 material.[41]

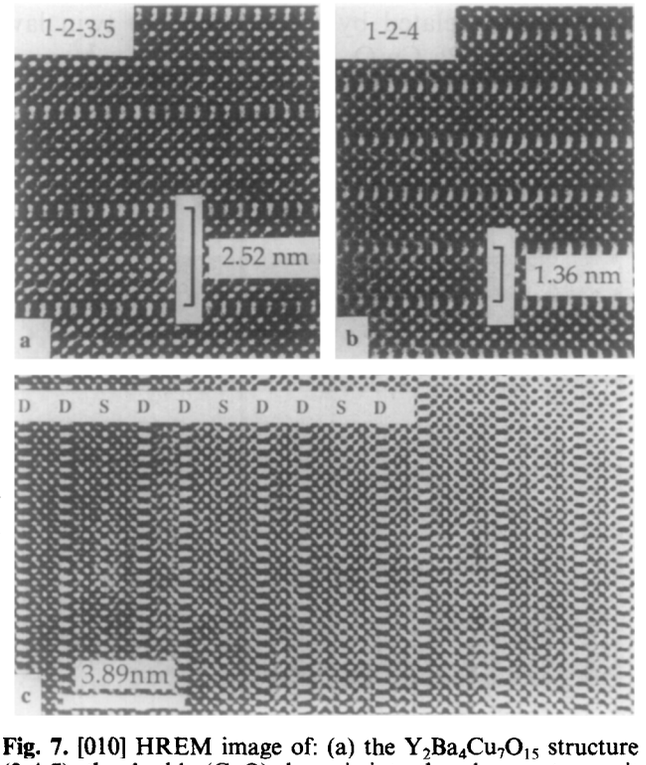

Fig. 7. [010] HREM image of: (a) the $Y_2Ba_4Cu_7O_{15}$ structure (2-4-7); the double $(CuO)_2$ layer is introduced every two unit cells; (b) the $YBa_2Cu_4O_8$ structure (1-2-4); the double $(CuO)_2$ layer is introduced every unit cell; (c) a complex sequence of double and single CuO layers.

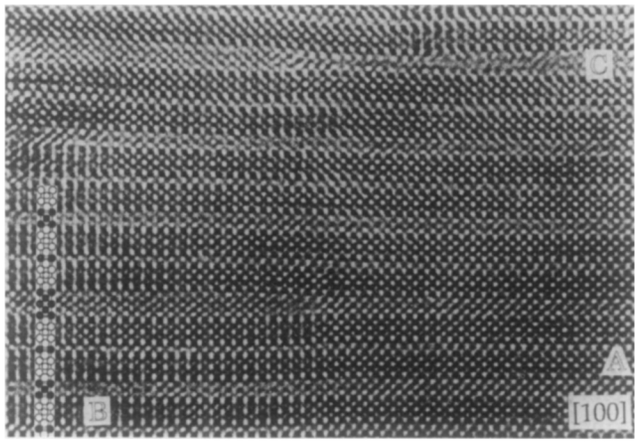

Fig. 8. Heavily distorted part of a 2-4-7 grain with all double $(CuO)_2$ layers replaced by triple ones (area A) or by quintuple ones (area B).

2.3 Cu substitution in YBCO 1-2-3 superconductors

Although it seems well established that superconductivity is to be associated with the CuO_2 layers, doping of the CuO-layers seems to play an important role in determining the concentration and the type of carriers. Also the critical temperature T_c is related to the composition of the CuO layer. It could for instance be shown that the 60 K plateau in the curve relating T_c to the oxygen content in this layer is associated with the presence of the $2a_o$ structure, i.e. with the material with ideal composition $YBa_2Cu_3O_{6.5}$.[44–46] It was attempted to replace copper in the CuO-layers, either completely or partly by other metallic ions such as iron, cobalt,

zinc, gallium. Also complex ions such as CO_3^{2-} or SO_4^{2-} were incorporated in the CuO-layer, carbon and sulphur occupying copper sites in the CuO chains. Iron substitution is found to induce a 'tweed' texture, the geometry of which could be assessed by assuming that iron occurs in the CuO layers in two types of oxygen coordination: octahedral and tetrahedral. The tetrahedrally coordinated iron ions induce microtwinning by the nucleation of CuO chains along mutually perpendicular directions which causes the tweed microtexture (ref. 47 and references therein). Cobalt substitutions in small concentrations has a rather similar aspect.[48]

The substitution of all copper ions in the CuO layers by gallium or cobalt ions ($YSr_2Cu_2MO_{7-x}$) leads to the formation of rows of corner sharing CoO_4 (or GaO_4) tetrahedra along the [110] direction of the basic perovskite structure, replacing in a sense the CuO_4 strings of square planar configurations along the b_o direction. The tetragonal symmetry is hereby reduced to an orthorhombic one.[49,50] The strings of tetrahedra can moreover adopt two mutually perpendicular directions giving rise to two twin related orientation variants of the orthorhombic structure. It was moreover shown that period doubling (also tripling) occurs in the (001) plane along the direction normal to the chains of tetrahedra. This could be rationalized by noting that the parallel chains can adopt two different configurations, differing by the sense of rotation of the coupled tetrahedra along a string. Period doubling can then be attributed to the regular alternation of these two types of chains in a parallel set.

In case of carbonate substitutions for Cu(1) in the $YSr_2Cu_3O_7$ compound, the CO_3 triangles align in chains along the perovskite b-axis.[51] We will discuss here a recent and similar substitution, the substitution by tetrahedral SO_4-groups in compounds with composition $[Y_{1-y}Sr_y]Sr_2[Cu_{3-x}(SO_4)_x]O_{7-\delta}$, where $y = 0{\cdot}16$ and $x = 0{\cdot}22$. The electron diffraction patterns of this material confirm this average structure determined by neutrons[52,53] but strong satellites are associated with every basic reflection. The [010] and [001] zone diffraction patterns of Fig. 9 shows the presence of bright first order satellites (Fig. 9(a)) and weaker second order satellites (Fig. 9(a, b)); the length of the satellite-**q**-vector is 1 nm^{-1}. The structure can therefore be considered as modulated with the wavevector in the (010) plane, inclined over an angle α ($\alpha \approx 32°$) with respect to the [100]-direction and with a wavelength $\lambda \approx 1$ nm. Although the observed modulation is orthorhombic, most [001] observed diffraction patterns show tetragonal symmetry, with superstructure spots along a^* as well as along b^*. This is due to the presence of two orthorhombic variants, related by the usual (110) twin law common in $YBa_2Cu_3O_{7-\delta}$.

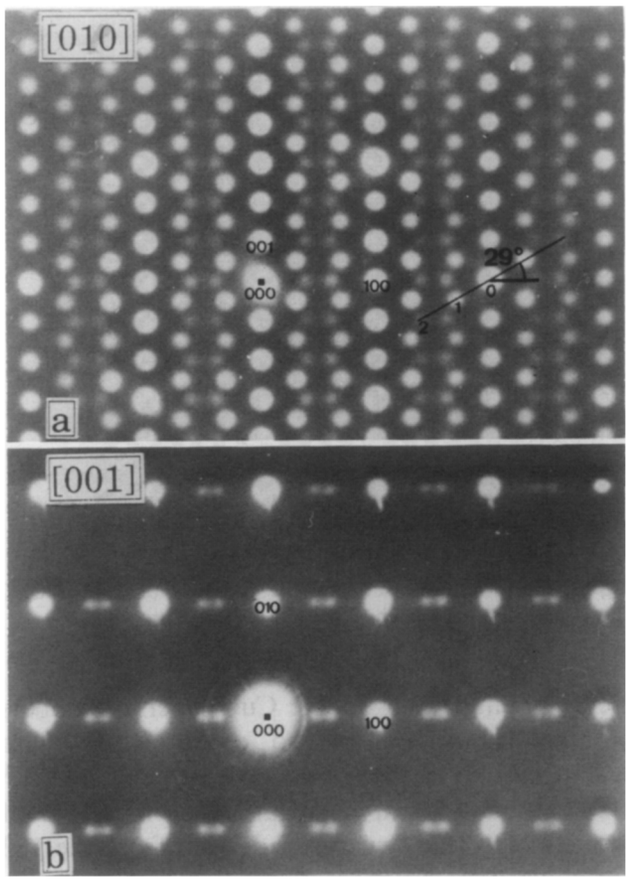

Fig. 9. Electron diffraction patterns of $[Y_{0{\cdot}84}Sr_{0{\cdot}16}]Sr_2Cu_{2{\cdot}78}(SO_4)_{0{\cdot}22}O_{6{\cdot}12}$: (a) [010] pattern showing satellites at every basic spot; numbers indicate spot order, the angle indicated is $\alpha = 29°$; (b) [001] pattern with only the weaker second order spots; indexing of both patterns refers to the basic unit cell.

High resolution images along the [010]-zone (Fig. 10), show the presence of a modulation corresponding to the satellites in the corresponding diffraction pattern of Fig. 9(a). The image is more

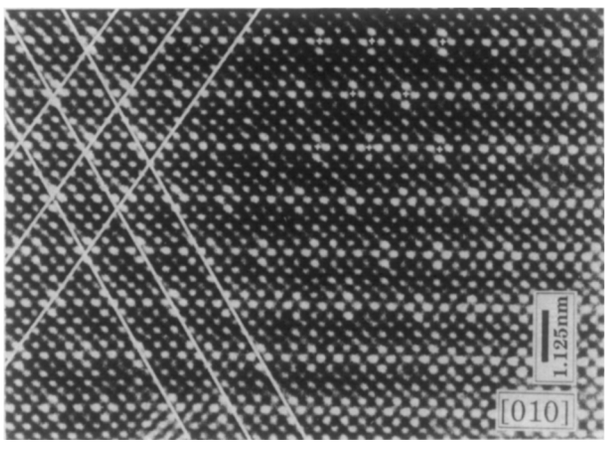

Fig. 10. High resolution image along the [010]-zone showing S-rich columns as brighter squares of four dots centered on the Cu(1)–S–O-layers. The maxima of the modulating wave, easily seen under grazing angles, are stressed by two sets of heavy lines in the image. The brighter dot configurations are indicated in part of the image by small crosses.

or less the same as that of the undoped $YBa_2Cu_3O_7$ material, however every three or four repeat distances along the *a*-direction, squares of more intense dots are present. According to image simulations, this is to be associated with the presence of SO_4-groups in the Cu-O(1) layer. Along the *c*-direction the stacking of these columns or 'chains' is usually staggered in such a fashion that their configurations in every second Cu(1)– S–O-plane coincide vertically. Within a single Cu(1)–S–O-plane the alternation is incommensurate but the intensity maxima are spaced roughly as ... – $4a_o$ – $3a_o$ – $3a_o$ ... . Looking along the directions indicated by heavy lines in Fig. 10, planes containing a high density of SO_4-clusters are revealed by a modulation in dot intensity. These planes can be considered as the maxima of a planar concentration wave. The normal to this concentration wave makes an angle α of about 30° with the [100]-direction and the length of the wavevector is about 1 nm.

These observations can be explained by a simple model of SO_4-chain formation and ordering. The [001] high resolution image suggests the presence of chains oriented along the *b*-direction, the nature of which must differ from that of CuO chains by their S content. The stacking-rule of the SO_4-rich chains can be derived from the observation of the concentration waves in Fig. 10:

(1) The SO_4-chains substitute these sites of the Cu(1)-sublattice which are closest to the maxima of the concentration waves.

(2) The integer *l*-coordinates of the second order satellites as well as direct observations in high resolution images suggest that the SO_4-chain-stacking coincides vertically in every second plane along the [001] direction.

These observations allow us to propose an atomistic model for the modulation in $[Y_{1-y}Sr_y]Sr_2[Cu_{3-x}(SO_4)_x]O_{7-\delta}$. In the schematic representation of Fig. 11 only the Cu(1) sublattice is shown; dashed lines are the maxima of the concentration waves with angles $\alpha = \pm 30°$ and $\lambda \approx 1$ nm. Due to the incommensurability of the basic lattice with the modulation, the ordering along the *a*-direction is essentially aperiodic, which is in agreement with the absence of periodic superstructure spots in the diffraction patterns. A physical explanation for the observed SO_4-chain arrangement is not straightforward but certainly involves a strain component. The chains occupied by SO_4^{2-}-ions cause cylindrically symmetrical stress fields as a consequence of the difference in size of the sulphur-ions and the copper-ions that they replace. Parallel chains thus interact by mutually repulsive elastic forces which depend on the separation *r* as $1/r$. The equilibrium configuration of such a set of repelling parallel chains, when confined to a finite area, or with a specified concentration, consists of a triangular array. With the restriction that the SO_4-chains can only be located at positions in the Cu(1)O-chain layers, the observed distribution of SO_4-chains is the one that yields the largest average separations between different chains.

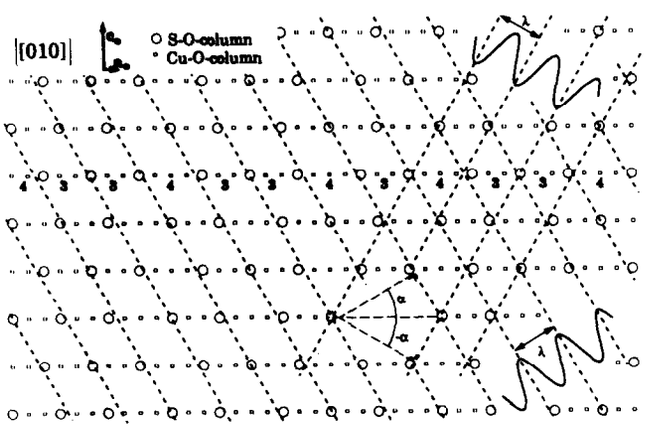

Fig. 11. Schematic representation of the incommensurate modulation of the Cu(1)-column-sublattice. Squares represent the Cu(1)-column sublattice, circles represent SO_4-chains and are located on Cu(1)-column-sites closest to the maxima of a SO_4-occupancy wave with wavevector inclined over α with respect to [100] and with wavelength λ.

3 Superconducting Bi-, Tl- or Hg-compounds

The Bi-compounds with general formula $Bi_2Sr_2Ca_nCu_{n+1}O_{6+2n}$ were the first to present T_c values above 100 K. They can be considered as a family of mixed layer compounds '2 2 *n n* + 1' and there is a clear correlation between the chemical formula and the values of T_c; 20 K for $n = 0$, 80 K for $n = 1$ and 105 K for $n = 2$.[54–57] The existence of such a family was initially predicted based on HREM observations of singular lamellae containing a number of CuO_2 layers deviating from the bulk composition. All of the Bi-compounds moreover exhibit an incommensurate one-dimensional deformation modulation, localized mainly within the BiO layers.[58] The modulation was attributed primarily to the misfit between the perovskite blocks and the BiO layers and the particular lone pair electronic configuration of the Bi^{3+}.[59] The one-dimensional modulation reduces the point symmetry of the compound from tetragonal to monoclinic in the 2201 compound and to orthorhombic in the 2212 or 2223 compound. As a result defects, i.e. modulation twins caused by the modulation and related by the lost symmetry elements may arise. The effect of the substitution of bismuth by lead on the modulation period and on the geometrical features of the modulation wave, resulting in a stabilization of the 2212 or the 2223 structure, has been studied almost exclusively by

means of EM. The modulated structure in the lead substituted compounds, differs from that in the pure Bi-compounds; whereas the modulation waves in successive layers are in anti-phase in the pure Bi-compounds, they are in phase in the lead substituted compounds. Figure 12 compares the modulation along the [010] zone axis for the undoped (Fig. 12(a)) and the Pb doped compound (Fig. 12(b)).

Recently several higher-order members of the Hg-based superconducting family $HgBa_2Ca_{n-1}Cu_nO_{2n+2+\delta}$ have been synthesized recently; the critical temperature reaches a maximum of 133·5 K for the $n = 3$ member of the family,[60] while for larger n values, T_c seems to decrease.[61] It was furthermore shown (not very unexpectedly) that T_c increases steadily with pressure at a rate of more or less 1 K/GPa. In this way Chu *et al.*[62] and Nunez-Regueiro *et al.*[63] were able to reach values such as 164 and 155 K (T_c onsets) for the Hg-1223 compound respectively. This strong pressure effect suggests that by the appropriate chemical doping, which would introduce a chemical pressure, T_c values of the order of 150 K would not be excluded at normal-external-pressure. Several substitutions in the Hg-plane as well as at the Ba- or the Ca-positions have been tried by the Caen group; they have led to the discovery of a series of new Hg-based superconducting compounds, which can be prepared under ambient pressure and which have a T_c up to 110 K.[64–68]

The structure of all members is similar; they contain rock salt like slabs $[(BaO)(HgO_\delta)(BaO)]$, alternating with perovskite slabs of the type $[(CuO_2)(Ca)]_{n-1}(CuO_2)$. The structure for different n-compounds is represented in Fig. 13; for increasing n-values an extra $[(CuO_2)(Ca)]$ slab is inserted, leaving the rest of the average structure unaltered. Although there is a strong similarity between the Hg- and the Tl-series, the occupation of the oxygen sites in the Hg-layers and the corresponding one in the Tl layers, are quite different.

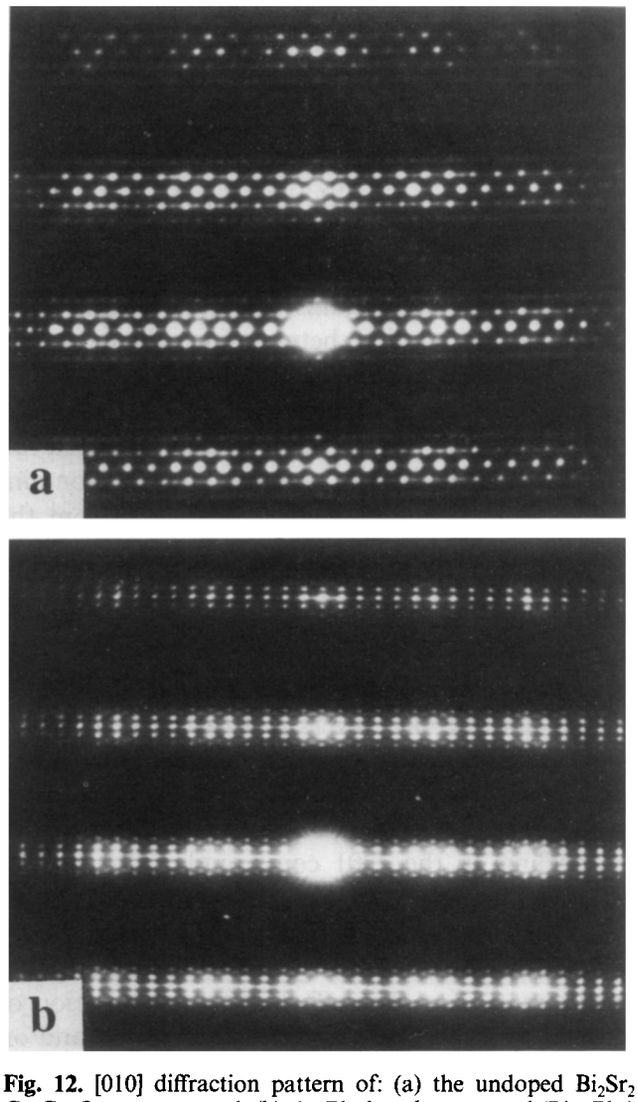

Fig. 12. [010] diffraction pattern of: (a) the undoped $Bi_2Sr_2Ca_1Cu_2O_{8+\delta}$+compound; (b) the Pb doped compound $(Bi_{2-x}Pb_x)Sr_2Ca_1Cu_2O_{8+\delta}$.

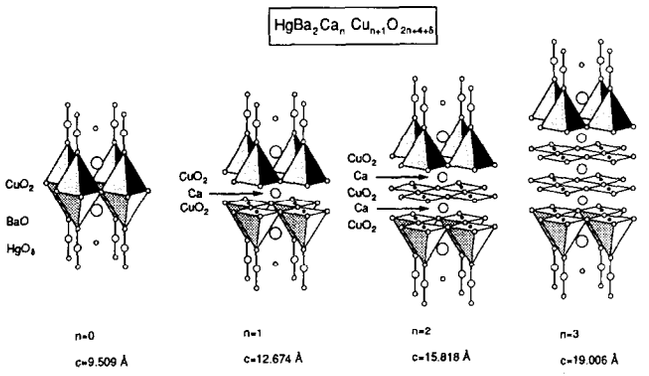

Fig. 13. Schematic representation of several members of the structural family $HgBa_2Ca_{n-1}Cu_nO_{2n+2+\delta}$.

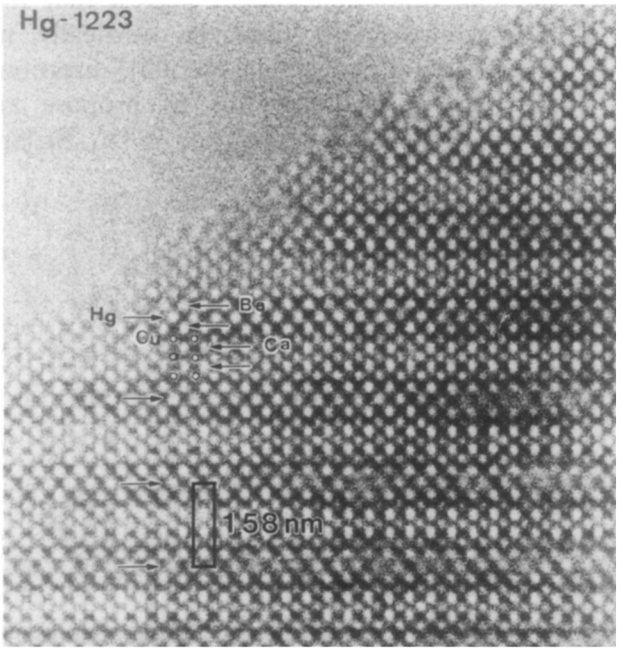

Fig. 14. High resolution image along [100] of $HgBa_2Ca_2Cu_3O_{8+\delta}$. In this contrast the heavy ions are imaged as bright dots; the imaging code as well as the unit cell is indicated in the figure.

HREM images of the different members of the family are obtained, particularly along the [100] zone, which is the most instructive one. An example for the 1223 compound is shown in Fig. 14; the cation configuration can be readily identified from symmetry considerations. There is clearly a one to one correspondence between the white dot configuration of the HREM image and the cation configuration of Fig. 13. This semi-intuitive interpretation has of course to be confirmed by computer simulations;[69] they will allow us to analyse in detail the atomic structure of planar defects in these compounds. The most common defect encountered, particularly for higher order members of the family, is the intergrowth of different n-members; they occur as isolated defects and are well known from other homologuous series. Periodicities up to $n = 8$ have been seen to occur locally, although no single phase material could be produced.[69] A most remarkable defect in this structure is the occasional occurrence of a double (HgO_δ) layer instead of the usual sequence of three layers [(BaO)(HgO_δ)(BaO)]. The occurrence of such defects with a double (HgO_δ) layer suggested the feasibility to produce '2 2 n–1 n' type materials; such '2 2 n–1 n' compounds have indeed been produced by replacing some of the Hg by Pr or Cu[70] or some of the Ca by a trivalent element such as e.g. Y.[71]

When Hg deficient compounds $Hg_{1-x}Ba_2Ca_{n-1}Cu_nO_{2n+2+\delta}$, with $x \approx 0{\cdot}3$ are prepared and carbon is introduced on the sublattice, T_c will decrease[72] and the carbonate groups will or substitute randomly for the Hg, as in the present compound or occur in an ordered way in related compounds.[73–75]

Electron diffraction as well as HREM of $Hg_{1-x}Ba_2Ca_2Cu_3O$ reveal the perfect 1223 structure, with no traces of superstructure or imperfections (see Fig. 15(b)). In the HREM image of Fig. 15 all

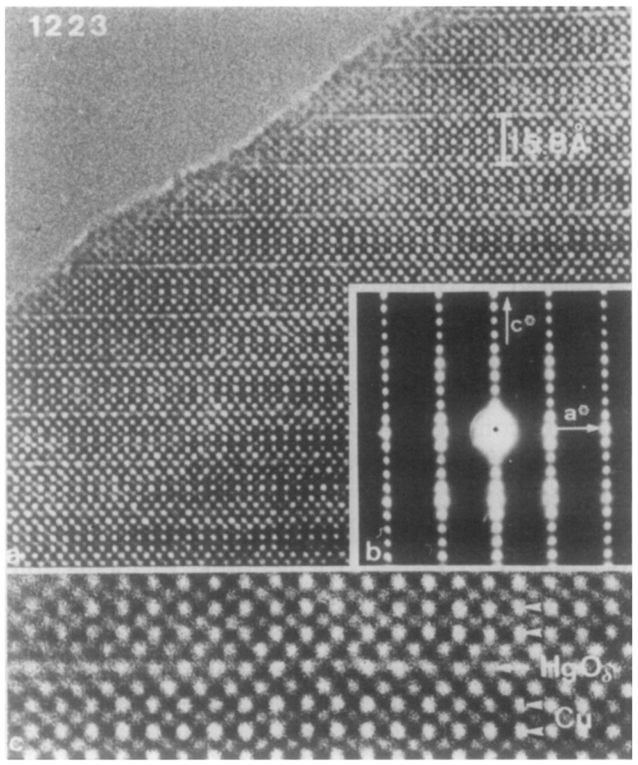

Fig. 15. (a) High resolution image along [010] of the Hg-1223 compound, showing the individual cation columns as bright dots. No extended defects are observed. (b) Corresponding electron diffraction pattern. (c) High magnification of part of (a); note that in the HgO_δ layer the intensity of the individual dots is not homogeneous.

cations are revealed as bright dots and the HgO_δ layer can easily be identified as the more diffuse layer; this follows by comparison with computer simulated images. Along this layer, however, we do see variations in the intensities of the different bright dots (see Fig. 15(c)) which is an enlargement of part of Fig. 15(a). We can quantify these variations by making densitometer traces along the HgO_δ layer as well as along one of the neighbouring CuO_2 layers. The results are shown in

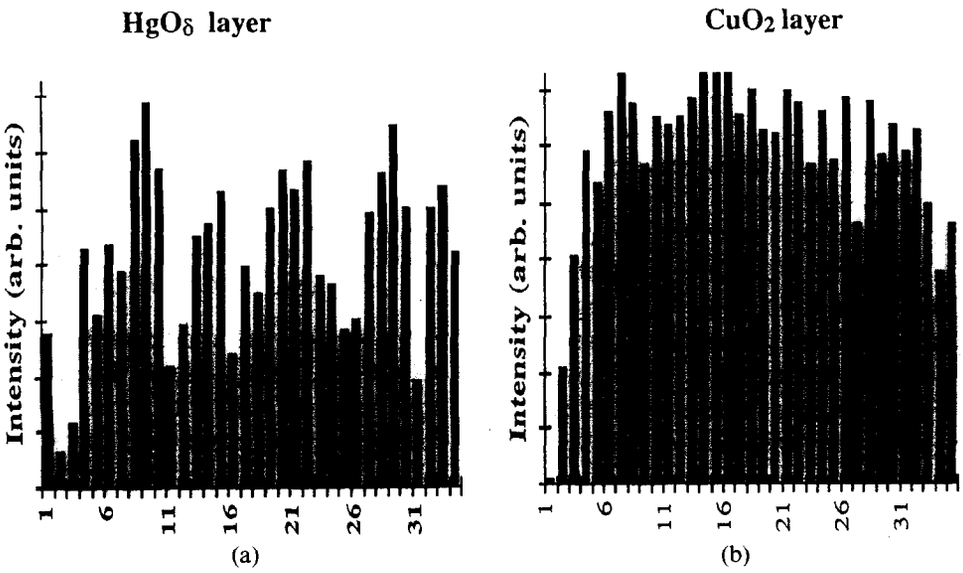

Fig. 16. Intensity measurement of individual dots from Fig. 15(c): (a) along the HgO_δ layer; (b) along the neighbouring CuO_2 layer.

Fig. 16(a), where we have plotted the intensity for different 'bright dots' along a single HgO_δ row; the intensities are corrected for the background. For the HgO_δ layer there is a clear, pseudo-periodic variation in the intensity (Fig. 16(a)), such variation is not observed in the corresponding measurement for the surrounding BaO or CuO_2 layer (Fig. 16(b)). These intensity variations are to be related to variations in the occupation of the Hg-sublattice. If the variations were not random but periodic, they would give rise to weak superstructure reflections visible in the diffraction patterns. If complete columns, or even a single one, were occupied by carbonate groups, this would be detected by HREM.[75,76] Measurements of the local composition by EDX, reveals a deficiency of Hg (0·7–0·8) with respect to the other elements, but no excess of Cu. We can therefore conclude that the Hg-deficiency is not compensated by an excess Cu. The missing Hg-ions are randomly distributed on the Hg-sublattice; they are most probably occupied by carbonate groups, by vacancies or by a mixture of both; this cannot be decided from EM only.

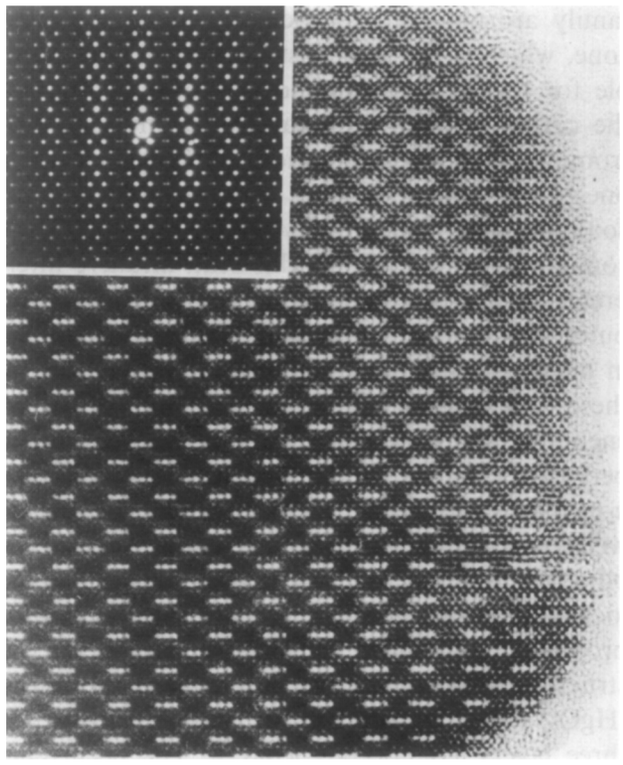

Fig. 17. HREM image of $Hg_{0.3}Tl_{0.7}Sr_{1.5}Ba_{2.5}Cu_2CO_3O_{7-\delta}$ along [100]; the carbonate groups are imaged as particularly white features. The corresponding diffraction pattern is shown as an inset.

4 Superconducting Oxycarbonates

A wide variety of novel superconducting materials has recently been prepared by incorporating complex ions such as carbonate, phosphate or sulphate groups in the perovskite-like structures of existing high T_c cuprates; for an overview and further references we refer to refs 77 and 78. Carbonate groups can be substituted into the mercury or thallium based cuprates of the type $Hg_{1-x}Tl_xSr_{4-y}Ba_yCu_2CO_3O_{7-\delta}$. The incorporation of these groups produces interesting modulated structures. Related compounds of the type $ASr_{4-y}Ba_yCu_2CO_3O_{7-\delta}$ where A = Tl, Hg or $Hg_{0.5}Pb_{0.5}$ were also found to exhibit remarkable long period interface modulated structures. The modulation vector is along the [010] perovskite direction in the samples with A = Tl and along the $[110]_p$ direction in the samples with A = Hg or A = $Hg_{0.5}Pb_{0.5}$. The wavelength is mostly incommensurate but varies between 6 and 8 times the basic perovskite unit.

High resolution electron microscopy of the compound $Hg_{1-x}Tl_xSr_{4-y}Ba_yCu_2CO_3O_{7-\delta}$, is able to directly image the modulation (Fig. 17). Together with the electron diffraction information (inset of Fig. 17) one can also deduce the origin of the modulation and the building blocks of the complex structure. The prominently bright dot sequences image columns of carbon and oxygen atoms which are the lightest atoms in the compound. The carbonate groups clearly substitute on the (Hg–Tl)-sublattice, in agreement with previous findings. The carbonate sequences contain either three or four dots. Bright and dark dot sequences alternate in anti-phase in successive layers, leading to a centered rectangular arrangement. The corresponding [100] zone diffraction pattern (Fig. 17) consists of main reflections, which can be indexed on a tetragonal lattice and weaker satellite reflections, which decrease in intensity with distance from the main reflections. The pattern looks commensurate, however careful measurements show that it is in fact incommensurate, the period being slightly smaller than $8b_P$. Actually the periodicity of the modulation can vary between $6b_P$ and $8b_P$, depending on a number of parameters, which will not be discussed here.

The high resolution images of these compounds not only suggest a model for the stacking along the *c*-direction:

$$[CO + (Tl, Hg)O] - (Sr, Ba)O - CuO_2 - (Sr, Ba)O - [(Tl, Hg)O + CO]$$

but also for the modulated structure within the [CO + (Tl, Hg)O]-plane. Incommensurate diffraction patterns originate from a structure in which commensurate carbonate strips of two different widths (3 and 4 times the perovskite unit) are uniformely mixed. The high resolution images (e.g. Fig. 17) give evidence for sequences such as 3434... or 334334....

As to the -near- future of HREM and the imaging of light elements in electron microscopy, we can announce that we have just installed a new CM30-FEG-Ultra twin microscope at the EMAT laboratory in Antwerp, which is able to produce structural information down to the 1·1 Å level. The interpretation of such images in function of the projected crystal potential is certainly not straightforward, but with the help of CCD recording and computer treatment of the data, we are starting real quantitative HREM.[79]

Acknowledgements

We are most grateful to S. Amelinckx (Antwerp) for common research on the YBCO-based compounds and to M. Huvé (now in Lille), M. Hervieu, C. Michel and B. Raveau (Caen), C. Chaillout and M. Marezio (Grenoble), C. Greaves (Birmingham) and E. V. Antipov (Moscow) for valuable discussions and use of common results on the Hg-based compounds and the oxycarbonates.

References

1. Van Tendeloo, G., Zandbergen, H. W. & Amelinckx, S., *Solid State Comm.*, **63** (1987) 389.
2. Zandbergen, H. W., Van Tendeloo, G., Okabe, T. & Amelinckx, S., *Phys. Stat. Sol.(a)*, **103** (1987) 45.
3. Cava, R. J., Hewat, A. W., Hewat, E. A., Batlogg, B., Marezio, M., Rabe, K. M., Krajewski, J. J., Peck, Jr., W. F., Rupp, Jr., L. W., *Phys. C*, **165** (1989) 419–33.
4. Ourmazd, A. & Spence, J. C. H., *Nature*, **329** (1987) 425–7.
5. Lin, Y. P., Greedan, J. E., O'Reilly, A. H., Reimers, J. N., Stager, C. V. & Post, M. L., *J. Sol. Stat. Chem.*, **84** (1990) 226–36.
6. Chaillout, C., Alario Franco, M. A., Capponi, J. J., Chenavas, J., Hodeau, J. L. & Marezio, M., *Phys. Rev. B*, **36** (1987) 7118–20.
7. Zhu, Y., Moodenbaugh, A. R., Suenaga, M. & Tafto, J., *Physica C*, **167** (1990) 363–8.
8. Chen, C. H., Werder, D. J., Schneemeyer, L. F., Gallagher, P. K. & Waszczak, J. V., *Phys. Rev. B*, **38** (1988) 2888–91.
9. Rao, C. N. R., Nagarajan, R., Ganguli, A. K., Subbana, G. N. & Bhat, S. V., *Phys. Rev. B*, **42**(4) (1990) 6765–8.
10. Burmester, C. P., Quong, S., Wille, L. T., Gronsky, R., Ahn, B. T., Lee, V. Y., Beyers, R., Gür, T. M. & Huggings, R. A., *Mat. Res. Soc. Symp. Proc.*, **183** (1990) 369–74.
11. Hodeau, J.-L., Bordet, P., Capponi, J.-J., Chaillout, C. & Marezio, M., *Phys. C.*, **153–155** (1988) 582–5.
12. Beyers, R., Ahn, B. T., Gorman, G., Lee, V. Y., Parkin, S. S. P., Ramirez, M. L., Roche, K. P., Vazquez, J. E., Gür, T. M. & Huggings, R. A., *Nature* **340** (1989) 619–21.
13. Alario-Franco, M. A., Chaillout, C., Capponi, J. J. & Chenavas, J., *Mat. Res. Bull.*, **22** (1987) 1685–93.
14. Alario-Franco, M. A., Chaillout, C., Capponi, J. J., Chenavas, J., & Marezio, M., *Phys. C*, **156** (1988) 455–60.
15. Hou, C. J., Manthiram, A., Rabenberg, L. & Goodenough, J. B., *J. Mater. Res.*, **5** (1990) 9–16.
16. Chaillout, C., Alario Franco, M. A., Capponi, J. J., Chenavas, J., Strobel, P. & Marezio, M., *Sol. Stat. Comm.*, **65**(10) (1987) 283–6.
17. Hervieu, M., Domengès, B., Raveau, B., Post, M., McKinnon, W. R. & Tarascon, J. M., *Mat. Lett.*, **8** (1989) 73–82.
18. Hervieu, M., Domengès, B., Michel, C., Provost, J. & Raveau, B., *J. Sol. State Chem.*, **71** (1987) 263.
19. Van Tendeloo, G., Zandbergen, H. W. & Amelinckx, S., *Sol. Stat. Comm.*, **63** (1987) 603–6.
20. Fleming, R. M., Schneemeyer, L. F., Galagher, P. K., Batlogg, B., Rupp, L. W. & Waszczak, J. V., *Phys. Rev. B*, **37** (1988) 7920–3.
21. You, H., Axe, J. D., Kan, X. B., Hashimoto, S., Moss, S. C., Liu, J. Z., Crabtree, G. W. & Lam, D. J., *Phys. Rev. B*, **38** (1988) 9213–6.
22. Zeiske, T., Holhwein, D., Sonntag, R., Kubanek, F. & Wolf, T., *Phys. C*, **194** (1992) 1–8.
23. Nakazawa, Y. & Ishikawa, M., *Phys. C.*, **158** (1989) 381–4.
24. Nakazawa, Y. & Ishikawa, M., *Phys. C.*, **162–164** (1989) 83.
25. Ueda, Y. & Kosuge, K., *Phys. C.*, **156** (1988) 281–5.
26. Cava, R. J., Batlogg, B., Chen, C. H., Rietman, E. A., Zahurak, S. M. & Werder, D., *Phys. Rev. B.*, **36** (1987) 5719.
27. Strauven, H., Locquet, J. P., Verbeke, O. B. & Bruynseraede, Y., *Sol. Stat. Comm.*, **65** 293–6 (1987).
28. Gerdanian, P., Picard, C. & Touzelin, B., *Physica C*, **182** (1991) 11.
29. Van Dyck, D., Condé, C. & Amelinckx, S., *Phys. Stat Sol. (a)*, **56** (1979) 327–34.
30. Krekels, T., Van Tendeloo, G., Amelinckx, S., Wagener, D., Buchgeister, M., Hosseini, S. M. & Herzog, P., *Physica C*, **196** (1992) 363–8.
31. Yang, S., Claus, H., Veal, B. W., Wheeler, R., Paulikas, A. P. & Downey, J. W., *Phys. C*, **193** (1992) 243–52.
32. Rusiecki, S., Bucher, B., Kaldis, E., Jilek, E., Karpinski, J., Rossel, C., Pümpin, B., Keller, H., Kündig, W., Krekels, T. & Van Tendeloo, G., *J. Less Common Metals*, **164–165**, (1990) 31–8.
33. Reyes-Gasga, J., Krekels, T., Van Tendeloo, G., Van Landuyt, J., Amelinckx, S., Brugginck, W. H. M. & Verweij, H., *Phys. C*, **159** (1989) 831–48.
34. Van Tendeloo, G. & Amelinckx, S., *J. El. Mic. Technique*, **8** (1988) 285–95.
35. Khachaturyan, A. G. & Morris, J. W., *Phys. Rev. Lett.*, **61** (1988) 215–8.
36. de Fontaine, D., Ceder, G. & Asta, M., *Nature*, **343** (1990) 544–6.
37. Zandbergen, H. W., Gronsky, R., Wang, K. & Thomas, G., *Nature*, **331** (1988) 569.
38. Morris, D. E., Asmar, N. G., Nickel, J. H., Sid, R. L., Wei, J. Y. T. & Post, J. E., *Physica C*, **159** (1989) 287.
39. Karpinski, J., Kaldis, E., Jilek, E., Rusiecki, S. & Bucher, B., *Nature*, **336** (1988) 660.
40. Bordet, P., Chaillout, C., Chenavas, J., Hodeau, J. L., Marezio, M., Karpinski, J. & Kaldis, E., *Nature*, **334** (1989) 596.
41. Krekels, T., Van Tendeloo, G., Amelinckx, S., Karpinski, J., Ruisiecki, S., Kaldis, E. & Jilek, E., *Physica C*, **178**, (1991) 383.
42. Krekels, T., Van Tendeloo, G., Amelinckx, S., Karpinski, J., Kaldis, E. & Ruisiecki, S., *Solid State Comm.*, **79**, (1991) 607.
43. Ramesh, R., Jin, S. & March, P., *Nature*, **346** (1990) 420.
44. Beyers, R., Ahn, B. T., Gorman, G., Lee, V. Y., Parkin, S. S. P., Ramirez, M. L., Roche, K. P., Vasquez, J. E., Gür, T. M. & Huggings, R. A., *Nature*, **340** (1989) 619.
45. Poulsen, H. F., Andersen, N. H., Andersen, J. V., Bohr, H. & Mauritsen, O. G., *Nature*, **349** (1991) 594.
46. Krekels, T., Zou, H., Van Tendeloo, G., Wagener, D., Buchgeister, M., Hosseini, S. M. & Herzog, P., *Physica C*, **196** (1992) 363.

47. Krekels, T., Van Tendeloo, G., Broddin, D., Amelinckx, S., Tanner, L., Mehbod, M., Vanlathem, E. & Deltour, R., *Physica C*, **173** (1991) 361.
48. Schmahl, W. W., Punis, A., Salje, E., Freeman, P., Graeme-Barber, A., Jones, R., Singh, K. K., Blunt, J., Edwards, P. P., Loram, J. & Mirza, K., *Phil. Mag. Lett.*, **60** (1989) 341.
49. Krekels, T., Milat, O., Van Tendeloo, G., Amelinckx, S. Babu, T. G. N., Wright, A. J. & Greaves, C., *J. Sol. State Chem.*, **105** (1993) 313.
50. Van Tendeloo, G. & Amelinckx, S., *Advanced Materials*, **5** (1994) 620.
51. Miyazaki, Y., Yamane, H., Ohnishi, N., Kajitani, T., Hiraga, K., Morii, Y., Funahashi, S. & Hirai, T., *Physica C*, **198** (1992) 7.
52. Slater, P. R., Greaves, C., Slaski, M. & Muirhead, C. M., *Physica C*, **208** (1993) 193.
53. Krekels, T., Milat, O., Van Tendeloo, G., Van Landbuyt, J., Amelinckx, S., Slater, P. R. & Greaves, C., *Physica C*, **210** (1993) 439.
54. Michel, C., Hervieu, M., Borel, M. M., Grandin, A., Deslandes, F., Provost, J. & Raveau, B., *Z. Physik B*, **68** (1987) 421.
55. Hazen, R. M., Prewitt, C. T., Angel, R. J., Ross, N. L., Finger, L. W., Hadidiacos, C. G., Veblen, D. R., Heaney, P. J., Hor, P. H., Meng, R. L., Sun, Y. Y., Wang, Y. Q., Xue, Y. Y., Huang, Z. J., Gao, L., Bechtold, J. & Chu, C. W., *Phys. Rev. Lett.*, **60** (1988) 1174.
56. Maeda, H., Tanaka, Y., Fukitoki, M. & Asano, T., *Jpn. J. Appl. Phys.*, **27** (1988) L205.
57. Zandbergen, H. W., Huang, Y. K., Menken, M. J. V., Li, J. N., Kadowaki, K., Menovsky, A. A., Van Tendeloo, G. & Amelinckx, S., *Nature*, **322** (1988) 620.
58. Zandbergen, H. W., Groen, W. A., Van Tendeloo, G., Van Landuyt, J. & Amelinckx, S., *Solid State Comm.*, **66** (1988) 397.
59. Zandbergen, H. W., Groen, W. A., Mijlhoff, F. C., Van Tendeloo, G. & Amelinckx, S., *Physica C*, **156** (1988) 325.
60. Schilling, A., Cantoni, M., Guo, J. D. & Ott, H. R., *Nature*, **363** (1993) 56.
61. Antipov, E. V., Lourciro, S. M., Chaillout, C., Capponini, J. J., Bordet, P., Tholence, J. L., Putilin, S. N. & Marezio, M., *Physica C*, **215** (1993) 1.
62. Chu, C. W., Gao, L., Chen, F., Huang, Z. J., Meng, R. L. & Xue, Y. Y., *Nature*, **365** (1993) 323.
63. Nunez-Regueiro, M., Tholence, J. L., Antipov, E. V., Capponi, J. J. & Marezio, M., *Science*, **262** (1993) 97.
64. Maignan, A., Van Tendeloo, G., Hervieu, M., Michel, C. & Raveau, B., *Physica C*, **212** (1993) 239.
65. Hervieu, M., Van Tendeloo, G., Maignan, A., Michel, C., Goutenoire, F. & Raveau, B., *Physica C*, **216** (1993) 264.
66. Pelloquin, D., Hervieu, M., Michel, C., Van Tendeloo, G., Maignan, A. & Raveau, B., *Physica C*, **216** (1993) 257.
67. Martin, C., Huve, M., Van Tendeloo, G., Maignan, A., Michel, C., Hervieu, M. & Raveau, B., *Physica C*, **212** (1993) 274.
68. Maignan, A., Michel, C., Van Tendeloo, G., Hervieu, M. & Raveau, B., *Physica C*, **216** (1993) 1.
69. Van Tendeloo, G., Chaillout, C., Capponi, J. J., Marezio, M. & Antipov, E. V., *Physica C*, **223** (1994) 219.
70. Martin, C., Hervieu, M., Van Tendeloo, G., Goutenoire, F., Michel, C., Maignan, A. & Raveau, B., *J. Sol. State Comm.*, (1995) 53.
71. Radaelli, P. G., *et al. Physica C*, (1995) in press.
72. Kopnin, E. M., Antipov, E. V., Capponi, J. J., Borded, P., Chaillout, C., de Brion, S., Maerzio, M., Bobylev, A. P. & Van Tendeloo, G., *Physica C*, (1995) 222.
73. Alario-Franco, M., Chaillout, C., Capponi, J. J., Souletie, B. & Tholence, J. L., *Physica C*, **222** (1994) 52.
74. Uehara, M., Sahoda, S., Nakata, H., Akimitsu, J. & Matsui, Y., *Physica C*, **222** (1994) 27.
75. Matusi, Y., Kawashima, T. & Takayama-Muromachi, E., *Physica C*, **235–240** (1994) 166.
76. Huvé, M., Van Tendeloo, G., Hervieu, M., Maignan, A. & Raveau, B., *Physica C*, **231** (1994) 15.
77. Hervieu, M., Michel, C., Van Tendeloo, G., Martin, C., Maignan, A. & Raveau, B., *Physica C*, **235–240** (1994) 25.
78. Raveau, B., Michel, C., Hervieu, M., Van Tendeloo, G., Martin, C. & Maignan, A., *Superconductivity*, **7** (1994) 9.
79. Van Dyck, D., Op de Beeck, M. & Coene, W., *Optik*, **93** (1994) 103.